

# Beyond Correlation: A Path-Invariant Measure for Seismogram Similarity

Joshua Dickey, Brett Borghetti, William Junek, and Richard Martin

April 2019

## ABSTRACT

Similarity search is a popular technique for seismic signal processing, with template matching, matched filters and subspace detectors being utilized for a wide variety of tasks, including both signal detection and source discrimination. Traditionally, these techniques rely on the cross-correlation function as the basis for measuring similarity. Unfortunately, seismogram correlation is dominated by path effects, essentially requiring a distinct waveform template along each path of interest. To address this limitation, we propose a novel measure of seismogram similarity that is explicitly invariant to path. Using Earthscope’s USArray experiment, a path-rich dataset of 207,291 regional seismograms across 8,452 unique events is constructed, and then employed via the batch-hard triplet loss function, to train a deep convolutional neural network which maps raw seismograms to a low dimensional embedding space, where nearness on the space corresponds to nearness of source function, regardless of path or recording instrumentation. This path-agnostic embedding space forms a new representation for seismograms, characterized by robust, source-specific features, which we show to be useful for performing both pairwise event association as well as template-based source discrimination with a single template.

# INTRODUCTION

Seismograms are time-series records of the earth’s motion at a fixed station. This motion results from seismic waves, that have often traveled a considerable distance from the source event, and seismograms reflect the combined influence of both the source itself, and the propagation path between source location and recording station (Bormann and IASPEI, 2012). As illustrated in Fig. 1, two seismograms depicting different events yet sharing a common path can appear similar. This fact has long been recognized by the seismic community (Stauder and Ryall, 1967; Kanamori and Ishida, 1978). In the earliest days of manual processing and helicorders, analysts were often able to identify mining events from a particular mine, recorded at a particular station, by simply comparing the visual similarity of new seismograms to previously recorded examples (Israelsson, 1990). In fact, a common practice was to take two translucent paper seismograms and compare them, by passing the waveforms across one another while holding them up to a light source (Schulte-Theis and Joswig, 1993). Thus began the science of seismogram similarity. Of course, the advent of computer processing ushered in the development of a multitude of techniques to exploit these similarities algorithmically. Case-based discrimination (Dysart and Pulli, 1987), template matching (Giannakis and Tsatsanis, 1990), waveform correlation (Harris, 1991), subspace detection (Harris, 2006) and similarity search (Yoon et al., 2015) are all similarity-based algorithms which have been proposed over the last several decades, and deployed against a wide range of seismic signal processing tasks, such as discriminating mining blasts, screening swarm events, identifying aftershock sequences, and even detecting general seismic signals.

While these algorithms have different tasks ranging from discrimination to detection, fundamentally they are all examples of similarity-based classifiers (Chen et al., 2009), which estimate the class label of a new seismogram based on its similarity to one or more previously labeled templates. Furthermore, these similarity-based classifiers all share a common measure of similarity: cross-correlation. Such methods are generally referred to as correlation detectors (Harris, 2006).

This common reliance on correlation is concerning, because the correlation coefficient of two seismograms is dominated by path effects (Schulte-Theis and Joswig, 1993), as demon-

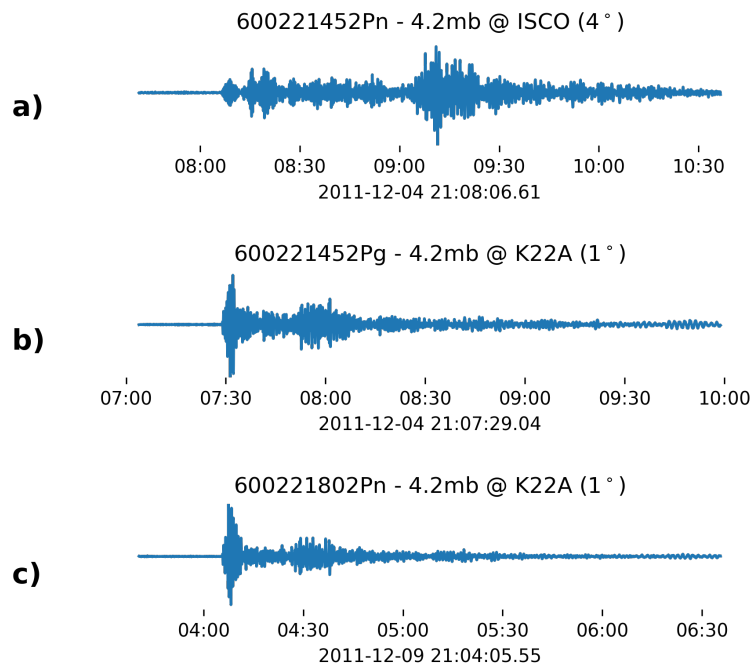


Figure 1: Three Seismograms depicting explosions at a coal mine near Thunder Basin, WY. Seismograms a) and b) depict a common source event (600221452), recorded at two separate seismic stations, ISCO and K22A respectively. Seismogram c) depicts a nearby event (600221802), also recorded at K22A. Seismograms a) and b) depict the same event recorded at different stations, while seismograms b) and c) depict different events which share a common path. The correlation between the same-source waveforms a) and b) is only 0.03, and the waveforms visually appear quite different. On the other hand, the visual similarity between the path-similar waveforms b) and c) is obvious, and they are correlated with a coefficient of 0.18. This illustrates the path-dominant similarity inherent to seismogram correlation.

strated in Fig. 1. While path-dominant similarity can be desirable, such as when detecting aftershock sequences from a particular fault, or mining blasts from within a small quarry, in general, path-dominant similarity is problematic, as source-similar signals de-correlate with even slight deviations in path (Harris, 2006). This includes deviations in origin location, such as two explosions occurring at different points in a mining quarry, and deviations in recording location, such as two recordings of the same explosion by separate seismic stations in a regional seismic array. In either case, path differences of even just a quarter wavelength can significantly degrade the correlation of two seismograms (C. Pechmann and Kanamori, 1982; Motoya and Abe, 1985).

This work presents a new measure for seismogram similarity that bypasses correlation entirely, and that is designed to be both path-invariant and source-specific. To be precise, the design goal is to create a measure of seismogram similarity that enables the identification of seismograms sharing a common source event, regardless of the path of travel. While such a measure was previously computationally intractable, it is possible with the careful application of deep convolutional neural networks (CNNs). In 2019, researchers at the Los Alamos National Laboratory published a method using a CNN to predict the pairwise association of seismic phase arrivals, for 6 second windows, across a local group of 6 stations in northern Chile, reporting an accuracy of over 80% (McBrearty et al., 2019). Building on these results, we construct a source-dominant, path-invariant measure for seismogram similarity which operates on 180 second windows and is generalized across more than 1,000 sensors across North America. We do this by utilizing a state-of-the-art machine learning technique from the field of facial recognition, called a Triplet Network, which not only indicates pairwise association between seismograms, but actually maps the seismograms to low-dimensional vectors, called embeddings, such that the embedding space distance between seismograms sharing a common source event are minimized, regardless of path, while remaining distinct from any other events. This embedding strategy is displayed in Fig. 2. In this way, the embedding function becomes a rich feature extraction technique for source-specific and path-invariant features.

The triplet network architecture accepts three observations - two similar and one different from the others. Training a triplet network to learn seismic source similarity requires source-

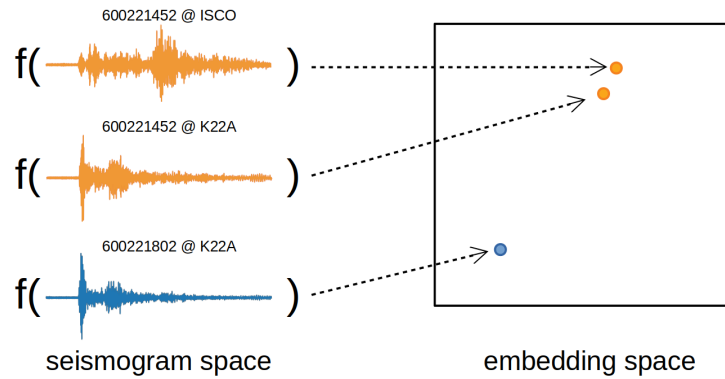


Figure 2: Path-Invariant Embedding Function for Seismograms. The embedding function,  $f(\cdot)$ , is a non-linear transformation that maps time-series seismograms to low-dimensional embeddings. The mappings should be path-invariant and source-specific, such that regardless of the recording station, all seismograms associated with a particular event are mapped closely in the embedding space, and seismograms not associated with that event have more distant embeddings, as demonstrated in this notional diagram. This embedding function can be learned using a convolutional neural network architecture, trained with seismogram triplets.

similar seismogram triples: two of the three waveforms are associated with a common source event and the third waveform is not. For this task, it is preferable to have a training set containing seismograms recorded from a densely-spaced sensor network, so that the neural network can experience seismograms recordings across numerous paths for the same event. The 400 three-channel broadband sensors of the USArray experiment provided an ideal dataset of seismograms; data from this array is used for training and testing. The triplet network is trained against 13 years of data (2007 - 2013), validated against a single year of data (2014), and tested against the final two years of data (2015-2016). Additionally, a subset of 51 recording stations and a small region of event locations was held out from the algorithm during training, to allow a proper evaluation of the generalizability of the technique. A map detailing the dataset is shown in Fig. 3.

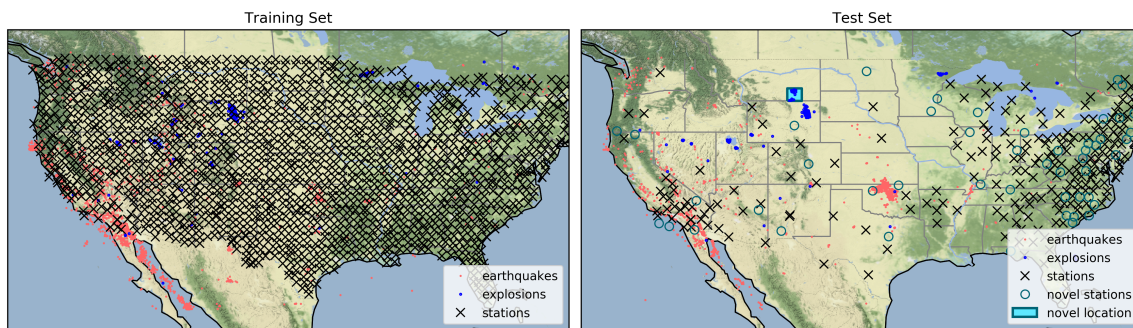


Figure 3: Map showing the geographical location of each recording station and event in the training and testing datasets. The majority of the stations were installed as part of the Earthscope’s Transportable USArray, and were in operation from 18 to 24 months before being moved. Additionally, 51 novel stations and a small region of novel event locations are unique to the test set.

The value of this path-invariant measure is demonstrated through performance evaluation on two common seismic tasks: event association, and source discrimination. The event association task of determining whether or not two waveforms depict the same event achieves a binary accuracy of 80%. This accuracy is achieved using only the waveform characteristics, without information on times or recording locations, and the technique has strong potential to augment existing methods of event association (McBrearty et al., 2019).

The real promise of the technique, however is for source discrimination. The embedding space is a rich basis for source-specific seismic feature extraction (Hadsell et al., 2006). Our similarity-based explosion discriminator achieves 95.8% accuracy with no explicit training for the source discrimination task; the discriminator simply compares the similarity of unknown waveforms to a single randomly-selected explosion template. This technique is often referred to as one-shot learning (Koch et al., 2015), and shows promise for discrimination of novel sources when only a few extant templates are available.

In the remainder of this work, these contributions and conclusions are explored in detail, by reviewing the related literature, outlining methodology, and detailing and discussing our results.

## BACKGROUND

This work merges two relatively disparate fields of science. On the one hand, the application is seismogram similarity, a field with a rich history and considerable previous research. On the other hand, the methodology employs learned similarity, a relatively nascent field that has principally been associated with machine learning image processing applications. This background section is divided into three distinct subsections: seismogram similarity; learned similarity; and learned seismogram similarity. Each subsection contains a brief background and literature review, as well as a discussion of the limitations and gaps in the current research, which our work attempts to fill.

### Seismogram Similarity

A seismogram represents the composition of several effects, including the seismic source itself, the propagation path from the source to the seismometer, the frequency response of the seismometer, as well as any ambient noise at the seismometer’s location (Bormann and IASPEI, 2012). Because of this diverse composition, estimating and even defining seismogram similarity can be quite challenging.

The traditional measure for seismogram similarity is the cross-correlation function. This measure has been used for detecting and discriminating seismic signals since the late 1980s (Dysart

and Pulli, 1987), and such techniques are commonly referred to as correlation detectors (Harris, 2006). Correlation detectors are exquisitely sensitive, allowing detections near the noise floor for known repeating events in highly confined geographical regions (Gibbons and Ringdal, 2006). Unfortunately, this confinement is also a limitation, as seismogram correlation has been shown to decay exponentially with even minor differences in path distance (Israelsson, 1990). In fact, early research suggested that correlation-based similarity was limited to signals with hypo-centres separated by no more than a quarter wavelength (Frankel, 1982; Motoya and Abe, 1985), although later efforts have since shown improvements, allowing the correlation length to be up to two wavelengths (Harris, 1991). Additionally, researchers have also shown that seismograms quickly decorrelate across small variations in mechanism and source function (Hutchings and Wu, 1990). These facts limit the applicability of the correlation detector to only the most repetitive sources that are confined to localized geographical regions (Harris, 2006).

To increase the applicability of the correlation detector, there have been numerous adaptations proposed. To address variations in ambient noise, narrow bandpass filters were applied (Israelsson, 1990). To address minor variations in mechanism, composite templates were employed, derived from linear combinations of several master templates representing a range of mechanisms (Harris, 1991). To address path effects, dynamic waveform matching was developed, introducing a non-linearity to the correlation, allowing relative stretching or squeezing of the template (Schulte-Theis and Joswig, 1993). Subspace detectors attempt to address all of these variations at once, with even more robust composite templates (Harris, 2006). Recently, efforts focused on a multiplicity of templates and a computationally efficient search across them (Yoon et al., 2015; Zhang and Wen, 2015; Beaucé et al., 2017; Bergen and Beroza, 2018b). These efforts have significantly increased the effectiveness of correlation-based detectors. In fact, for regions with a high sensor density, such as Northern California, it is estimated that more than 90% of events have sufficient similarity to be detected via correlation (Waldhauser and Schaff, 2008). However, this figure is highly dependent on both the density of the sensor network and the completeness of the template library (Tibi et al., 2017). As such, Dodge and Walter estimate that still only 18% of all global events possess sufficient similarity to be detected by these methods (Dodge and Walter, 2015).



In summary, cross-correlation is a powerful measure for seismogram similarity, especially as a tool for detecting highly-repeating path-specific events. However, cross-correlation is fundamentally limited as a general measure of seismogram similarity, due to its inherent path-dependence. In this study, we address this limitation directly, and propose an alternative measure of seismogram similarity that is invariant to path, instrumentation and ambient noise.

## Learned Similarity

Each of the traditional seismogram similarity measures discussed so far has been fundamentally built around the cross-correlation function. However, it is interesting to note that almost none of those measures performed cross-correlation directly on the raw waveforms. Instead, each measure first applied some pre-processing function to the raw waveforms, either linear (time shifts, bandpass filters, linear combinations) or non-linear (dynamic time warping) prior to performing cross-correlation. We can generally understand these pre-processing functions to be mappings, from raw waveform space to a new *embedding space*. In each case, the mapping function is chosen such that the cross-correlation of two objects in the embedding space meets some desired similarity objective.

As it turns out, this embedding process used in traditional correlation-based similarity closely mirrors the process accomplished in machine learning-based similarity. For learned similarity, a parameterized embedding function architecture is established, and the parameters are optimized such that the distance between two objects in the space achieves the desired similarity objective. Over the last several years, such learned similarity measures have revolutionized the field of facial recognition in particular and the field of image processing in general, fueling advances in image recognition (Wang et al., 2014), object tracking (Leal-Taixe et al., 2016) and even vision navigation (Kumar et al., 2016). In the remainder of this section, we review some of the state of the art techniques available for constructing deep learned similarity measures, focusing particularly on the embedding function architecture and similarity objective, in turn.

## *Embedding Function Architecture*

Many early efforts to create learned similarity spaces utilized a linear architecture, such as the Mahalanobis distance (Xing et al., 2002; Jain et al., 2008, 2009). However, in recent years, much success has been gained by employing non-linear architectures (Belkin and Niyogi, 2003), particularly in the form of deep convolutional neural networks or CNNs (Hadsell et al., 2006). These CNNs were originally developed with 2-dimensional kernels, or filters, which allowed them to closely model the hand-crafted kernels traditionally used in image processing (LeCun et al., 1989). To adapt these powerful CNN architectures to process time-series waveforms, 1-dimensional CNNs were developed (Burges et al., 2003), enabling learned similarity spaces for audio waveforms (Jang and Yoo, 2009).

A more recent advancement to the traditional CNN architecture is the Temporal Convolutional Network (TCN), which is characterized by layered stacks of dilated causal convolutions and residual connections (Bai et al., 2018), as illustrated in Fig. 4. Such an architecture is particularly applicable to time-series waveforms with long-period dependencies, and offers several distinct advantages for seismic feature extraction (Dickey et al., 2019), including:

- Residual connections allow the model to have high-capacity and stable training.
- Dilated convolutions allow precise control over the receptive field.

The receptive field is of primary importance for time-series modeling, as it explicitly limits the learnable feature periodicity at a given layer. The equation for calculating the receptive field,  $r$ , for a given convolutional layer,  $l$ , kernel size  $k$ , and dilation rate,  $d$  is given in (1):

$$\begin{aligned} r_l &= r_{l-1} + d(k - 1) \\ \text{where } r_0 &= 0 \end{aligned} \tag{1}$$

In summary, the TCN is ideally suited for the efficient embedding of seismograms. This architecture presents a rich search space for learning an optimal embedding function. However, optimizing this function requires defining a suitable similarity objective, detailed next.

### *Similarity Objective*

Defining a quantitative similarity objective begins with a qualitative understanding of what similarity means for the given task, which is often referred to as a semantic definition of similarity. Once the semantic definition is established, the next step is to approximate it with an embedding function, such that nearness in the embedding space implies the semantic similarity (Chopra et al., 2005). This embedding function is learned via back-propagation of loss,  $\mathcal{J}$ , that reinforces the semantic definition.

One of the simplest semantic definitions of similarity is the concept of a *match*, where a matched pair of objects share a common identity, and an unmatched pair objects have different identities. For example, in the facial recognition task, a matched pair is defined as two images of the same person and an unmatched pair is defined as two images of distinct persons. The similarity objective is to optimize the parameters of the embedding function such that the embedding space distance between matched pairs is small, while the distance between unmatched pairs is large. This embedding function can be learned directly by a Siamese Neural Network, which takes in a batch of  $m$  object pairs, of which half are matched, and half are unmatched. The two objects,  $X_A^{(i)}$  and  $X_B^{(i)}$ , are then embedded via twin copies of the embedding function,  $f(\cdot)$ , with tied parameter weights  $w$ . The parameters of the embedding function are updated via the contrastive loss function, which penalizes two contrasting cases: matched pairs are penalized for being embedded too far apart and non-matched pairs are penalized for being embedded too close together with respect to some margin,  $\alpha$ , as given in Eq. (2) and Eq. (3), respectively (Chopra et al., 2005).

$$\mathcal{J} = \sum_{i=1}^{m/2} \left[ \left\langle f(X_A^{(i)}), f(X_B^{(i)}) \right\rangle \right] \quad (2)$$

$$\mathcal{J} = \sum_{i=1}^{m/2} \left[ \alpha - \left\langle f(X_A^{(i)}), f(X_B^{(i)}) \right\rangle \right]_+ \quad (3)$$

where  $[\ ]_+$  indicates the ramp function.

This technique works well, however, one drawback is the relatively inefficient use of the embedding space. Matches are too greedy, as the Siamese Network attempts to map all matches to a single point in the space. Meanwhile, non-matches are inefficient, pushed apart

only a fixed distance (Hoffer and Ailon, 2015). As a result, the Siamese Network is used less frequently in favor of the Triplet Network, which we shall next discuss.

The Triplet Network is similar to the Siamese Network (Hoffer and Ailon, 2015), however it is trained on batches of  $m$  triples, where each triple is comprised of an anchor object,  $X_A^{(i)}$ , a positive object,  $X_P^{(i)}$ , and a negative object,  $X_N^{(i)}$ . From within each triple, both a matched and non-matched pair can be constructed, however, the triplet loss function computes the relative embedding distance between the matched pair and non-matched pair, and no loss is accrued as long as the matched pair is closer by some margin,  $\alpha$ , as given in Eq. (4).

$$\mathcal{J} = \sum_{i=1}^m \left[ \left\langle f(X_A^{(i)}), f(X_P^{(i)}) \right\rangle - \left\langle f(X_A^{(i)}), f(X_N^{(i)}) \right\rangle + \alpha \right]_+ \quad (4)$$

where  $[ ]_+$  indicates the ramp function.

The Triplet network avoids the greediness of the Siamese network, and makes more efficient use of the embedding space, however it has its own drawbacks. Particularly, it can converge quickly at first, but learning slows rapidly, as the majority of the negative pairs are pushed beyond the margin, failing to train the weights appreciably. This can be solved by sampling hard pairs, semi-hard pairs and several other sampling strategies, all of which rely on iterative processing via forward propagation to determine embedding space distances, selectively sampling based on those distances, and then applying back propagation on the sample (Hermans et al., 2017). The algorithm used to sample hard pairs is commonly referred to as the *batch hard* loss function, and it requires that each batch be composed by randomly sampling  $L$  distinct identities and then randomly sampling  $K$  examples of each identity. In this way, the total number of objects in a batch is  $L * K$ , and each object is double indexed so that object  $X_u^{(v)}$  represents the  $u_{th}$  example of the  $v_{th}$  identity. The triplet loss is calculated using Eq. (4), except that in this case, every object in the batch is treated as an anchor  $X_A^{(i)}$ , and used to form a new triplet by selecting the *hardest* positive and *hardest* negative

samples,  $X_P^{(i)}$  and  $X_N^{(j)}$  respectively, for that anchor within that batch, as detailed in Eq. (5).

$$\mathcal{J} = \sum_{i=1}^L \sum_{A=1}^K \left[ \overbrace{\max_{\substack{P=1\dots K \\ P \neq A}} \langle f(X_A^{(i)}), f(X_P^{(i)}) \rangle}^{\text{hardest positive}} - \overbrace{\min_{\substack{j=1\dots L \\ N=1\dots K \\ j \neq i}} \langle f(X_A^{(i)}), f(X_N^{(j)}) \rangle}^{\text{hardest negative}} + \alpha \right]_+ \quad (5)$$

where  $[ ]_+$  indicates the ramp function.

## Deep Seismogram Similarity

Deep Neural Networks are now being used across many areas of seismological research, from earthquake detection to earthquake early warning systems, ground-motion prediction, seismic tomography, and even earthquake geodesy (Kong et al., 2018). However, no effort has been made to date to use deep neural networks to build a seismogram similarity metric. The closest related work was in early 2019, where researchers at Los Alamos National Labs published a paper describing a convolutional neural network for the pairwise association of seismograms depicting a common event, regardless of path (McBrearty et al., 2019). This work shows that path-invariant features do exist within the seismogram record. The seismograms considered in their work had a signal length of 6 seconds, and were restricted to recordings from 6 seismic stations. To process the signals, they used a shallow CNN with 4 layers, the input accepting two seismograms, the output producing a single boolean. This results in a similar output to a Siamese network, but without tied weights. The lack of tied weights means there is no embedding layer, which prevents their technique from being used for feature extraction. And the small number of stations limits the generalizability and transportability of their algorithm. Finally, the short signal length (6 s) limits each individual seismogram to containing a single phase arrival, thereby limiting its ability to extract long-period features, such as P and S wave energy ratios, which are particularly pertinent to general source discrimination tasks.

# METHODOLOGY

We present a novel seismogram similarity measure, based on a learned embedding function, that is both source-dominant and path-invariant. We show that the resultant embedding space is a rich representation space for seismic signals, useful for performing similarity-based classification against two common class dichotomies for seismograms: common event vs different events (event association) and earthquake vs explosion (source discrimination). The remainder of this section describes the embedding function architecture, the similarity objective, the USArray dataset and the evaluation criteria for the two classification tasks.

## Embedding Function Architecture

The goal is to learn a path-invariant embedding function for seismograms, useful for source discrimination at up to regional distances. This is accomplished using a hybrid architecture with two distinct parts: First, a TCN is employed with a receptive field wide enough to capture both P and S wave phases; second, a densely connected output layer, with 32 nodes, is employed to facilitate a rich low-dimensional embedding space.

Table 1: TCN Layer Parameters

| <b>l</b> | <b>k</b> | <b>d</b> | <b>Receptive Field</b> |
|----------|----------|----------|------------------------|
| 1        | 16       | 2        | 31                     |
| 2        | 16       | 4        | 91                     |
| 3        | 16       | 16       | 331                    |
| 4        | 16       | 256      | 4171                   |

Using Eq. (1), the TCN is designed to have an overall receptive field of 4171 samples (104 seconds), allowing it to learn long-period features down to 0.01 Hz, with just four dilated convolutional layers, as shown in Table 1. The TCN architecture consists of two residual stacks, shown in Fig. 4, each with 50 filters and a kernel size (filter length) of 16 samples. Finally, the TCN output is encoded by a densely connected output layer with 32 nodes, and the final output vector is normalized to have unit length. This results in 553,835 trainable parameters, and a network which reduces the three-channel 21,600 dimensional input into

just 32 dimensions, for a 99.9% reduction in dimensionality.

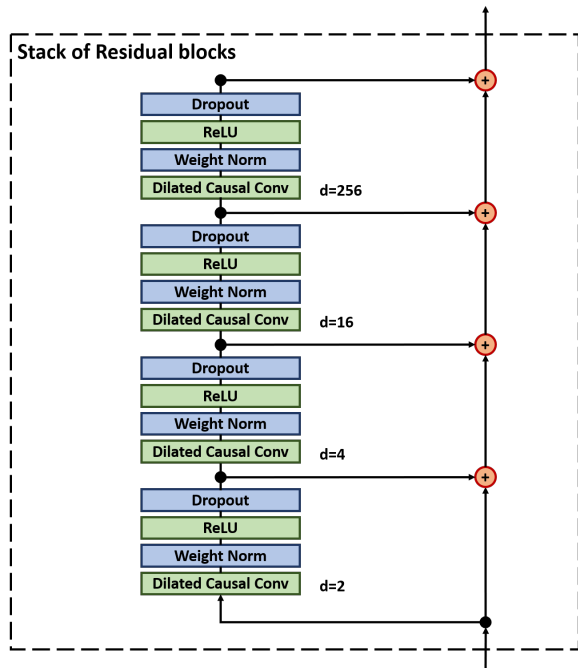


Figure 4: A single stack of 4 dilated residual blocks commonly found in a Deep Temporal Convolutional Neural Network Architecture. In this case, the residual blocks have exponentially increasing dilation rates, increasing from 2 to 256 across the 4 blocks. This rapid dilation provides the network a wide receptive field which is critical for learning long-period features frequently found in time-series waveform data.

## Similarity Objective

This embedding function is learned via a Triplet Network with batch-hard loss. Specifically, the batch size was set at 100, with  $L$  (the number of distinct source events in a batch) and  $K$  (the number of seismogram recordings for each event in a batch) both set equal to 10. In this way, each batch consists of 100 randomly selected seismograms, evenly represented across 10 different source events. These values were selected primarily on the basis of availability, since increasing  $K$  beyond 10 would have limited the dataset ( 95% of the events in the USArray dataset were recorded by at least 10 stations), and increasing  $L$  beyond 10 would require more memory than the 12Gb available in the Nvidia 1080Ti GPU used for training.

Embedding space distances are computed using the  $L_2$  Norm. Because the output of the embedding function is normalized, the embedding space vectors are all constrained to a hypersphere with radius = 1. This ensures a bounded distance between any two embeddings, as chord lengths are always bounded by  $[0,2]$  for any unit hypersphere. Because these pairwise distances are bounded, a fixed margin can be used throughout training (Sidiropoulos, 2014). In this work, the margin is fixed at  $\alpha = 0.2$ , which is common (Schroff et al., 2015).

## Data Collection

Learning a path-invariant measure for seismogram similarity requires a training dataset with many recordings of a single seismic event across many disparate paths. This is best accomplished by a dense network of seismometers across a wide region. EarthScope’s USArray dataset is ideally suited for this endeavor. In particular, we utilize two EarthScope observatories, the Transportable Array and the Reference Array, as the basis for our Training and Test Sets, respectively.

The USArray Transportable Array (TA) consists of 400 temporary seismic instruments that were deployed at more than 2,000 temporary station locations across the Continental US between 2007 and 2015 (Busby et al., 2018). Each station utilized a broadband 3-channel (North-South, East-West and Vertical) instrument, installed in a post-hole configuration and digitized at 40 Hz. The instruments were generally one of three types, Guralp CMG3T, Quantera STS, or Nanometrics Trillium; the digitizers were primarily Kinometrics Q330, Q680 or RefTek. In this work, our training and validation datasets are taken from the full array of TA seismograms, minus a random subset of 51 stations and a region of events located near the Rosebud mine in Montana, which were held out for testing. The training and validation sets were distinct in time, covering the periods from 2007-2013 and 2014, respectively. Associated arrival times were obtained by querying the ISC reviewed catalogs for any Continental US (CONUS) events over this period, resulting in 149,036 seismogram recordings of 4,825 distinct seismic events for the training set, and 22,561 seismogram recordings of 1,175 distinct seismic events for the validation set. A map detailing the layout of the training stations is shown in the left plot of Fig. 3.

The USArray Reference Array (REF) consists of 120 permanent seismic instruments



deployed across the Continental US, utilizing similar equipment as the Transportable Array. In this work, our test set is taken from the full array of TA and REF stations available from 2015 and 2016. Associated arrival times were obtained by querying the ISC reviewed catalog for CONUS events, resulting in a test set with 35,694 seismogram recordings of 2,452 distinct seismic events. All of the events in the test set are mutually exclusive with the training and validation data. Additionally, because of the stations and locations held out during testing, 6,934 of these seismograms were recorded by the 51 novel stations, and 87 seismograms represent events from the novel location near the Rosebud mine in Montana. Performance is evaluated explicitly on these novel data to explore the power and generalization of the technique.

All three datasets, training, validation and test, were limited to events with near CONUS epicenters, as defined by the following limits on latitude and longitude:  $25 < \text{LAT} < 50$ , and  $-125 < \text{LON} < -75$ . This accomplishes two purposes. First, this produces a catalog with more balanced samples of explosions and earthquakes, 207,291 and 26,568 respectively. Second, this restricts the study to regional signals. Regional signals are preferred due to the more manageable window length requirements vs teleseismic signals, as well as because the regional association task is much more interesting than the teleseismic association task; teleseismic signals recorded by such a dense regional network look much more similar even using traditional seismic similarity. We leave the exploration of this technique against teleseismic signals to future work. For completeness, we also have included histograms of seismogram station-to-event distances as well as event magnitudes for both the test and training sets, shown in Figs. 5 and 6, respectively.

For each of the 207,291 seismograms in the combined datasets, a 180-second window is selected which includes the 30 seconds prior to the cataloged arrival time and the 150 seconds subsequent to the arrival. The only pre-processing applied to the raw data was a normalization and de-trending. This window size was chosen so as to ensure the presence of both P and S waves within the window. While, this long window does present the opportunity for multiple arrivals within a single window, investigation shows that this occurs in only 0.15% of the seismograms in the dataset, and its effects are negligible on our results.

To create the training and validation triples, a generator function randomly selects an

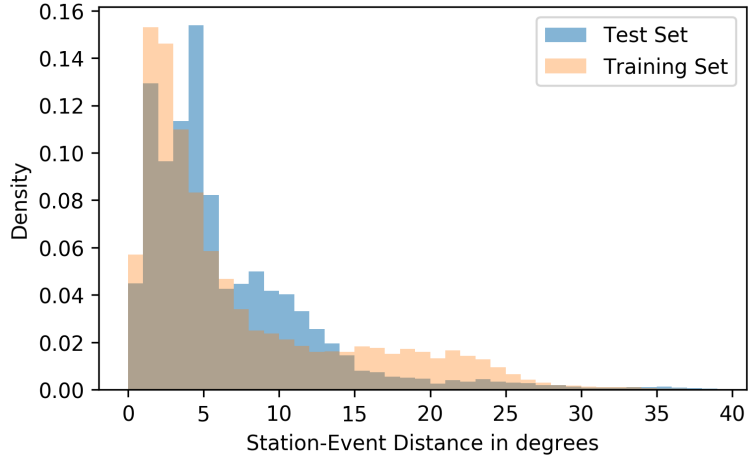


Figure 5: Histogram showing the distributions of station-event distances for all seismograms in the test and training sets. The distributions show that the test and training sets are similar, and that the majority of the seismograms in the combined dataset were recorded within 15 degrees of the epicenter.

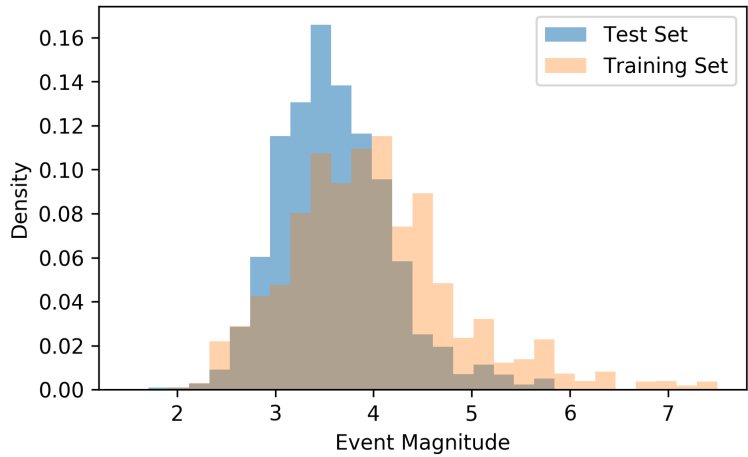


Figure 6: Histogram showing the distributions of event magnitudes for all seismograms in the test and training sets. The distributions show that the test and training sets are similar, and that the majority of the events in the combined dataset have a magnitude between 2 and 5 Mb.

anchor, as well as positive (same event, different station) and negative (different) events. Due to multiple site recordings of many of the individual events (on average, each event was recorded by 30 different stations), there are upwards of 300 million possible triples, which makes this a robust training set for learning seismogram similarity.

## Evaluation Criteria

To demonstrate the performance of the similarity measure, it is applied to two tasks: pairwise event association and source discrimination. Evaluation criteria for each of these tasks is shown below.

Event association is the process of correctly associating the arriving seismic phases of a single event across a network, and is a critical step in seismic analysis. The traditional algorithms used for this task have always been based on travel times and earth velocity models, however our method is similarity-based: we associate the seismograms entirely based on their pairwise similarity in the embedding space, with no external information about arrival times or recording locations. This is a binary classification task: given a pair of seismograms,  $X_A$  and  $X_B$ , the algorithm must classify the pair as matched or unmatched, where a matched pair is defined as two seismogram recordings of the same event. Classification is accomplished by comparing the similarity-based test statistic,  $S$ , against a user defined threshold,  $\tau$ , as seen in Eq. (6).

$H_0$ : UNMATCHED ( $X_A$  and  $X_B$  depict distinct events)

$H_A$ : MATCHED ( $X_A$  and  $X_B$  depict a common event)

$$S = \frac{1}{\langle f(X_A), f(X_B) \rangle} \tag{6}$$

reject  $H_0$  if  $S \geq \tau$

To report performance, a receiver operating characteristic (ROC) curve is built by varying  $\tau$  across the full range of  $S$ , and plotting the rate of false positives against the rate of false negatives for each  $\tau$ . Additionally, for the threshold  $\tau$  which maximizes accuracy, area under the ROC curve (AUC), binary classification accuracy, precision and recall are shown. The evaluation is performed across 50,000 random pairs of seismograms drawn from the test set,

and compared directly against the results found in (McBrearty et al., 2019). The results are also explored with respect to a subset of novel stations and events that were withheld during training, in order to better understand the abilities and limitations of the technique.

The source discrimination task is also formulated as binary classification, where unlabeled seismograms  $X$  are classified as either explosion or earthquake, based on their embedding space similarities to both the centroid of a set of explosion templates,  $X_{EXP}$  and the centroid of a set of earthquake templates,  $X_{EQK}$ . This is shown in Eq. (7), where  $\epsilon$  is machine precision.

$H_0$ : EARTHQUAKE ( $X$  depicts an earthquake)

$H_A$ : EXPLOSION ( $X$  depicts an explosion)

$$S = \frac{\langle f(X), f(X_{EQK}) \rangle}{\langle f(X), f(X_{EXP}) \rangle + \epsilon} \quad (7)$$

reject  $H_0$  if  $S \geq \tau$

The source discrimination test is performed against the full 35,694 seismograms in the test set. The ROC curve, AUC, accuracy, precision, and recall are presented.

Additionally, the performance of our similarity-based discriminator is directly compared to that of two state-of-the-art methods: the SVM-based discriminator proposed in (Kortström et al., 2016) and a CNN-based discriminator adapted from the work of (Nakano et al., 2019). In particular, our SVM and CNN implementations both utilize 20,000 training waveforms sampled evenly between explosions and earthquakes from the training set. The SVM uses 36 features, composed of nine frequency bins ([1-3 Hz], [2-5 Hz], [4-7 Hz], [6-9 Hz], [8-11 Hz], [10-13 Hz], [12-15 Hz], [14-17 Hz], [16-19 Hz]) and four time divisions (P, P coda, S and S coda), with the S-P time differences based on the iasp91 velocity model. The CNN uses high-resolution spectrogram images, as described in (Nakano et al., 2019).

## RESULTS

In this section, we report the performance of our similarity measure across two common tasks in seismology: pairwise event association and template-based source discrimination.

We also examine the computational requirements for implementing this method with respect to existing ones.

## Pairwise Event Association

To demonstrate that event association using this technique is possible, a special test set is created by sampling 50,000 pairs of seismograms from the test set, including 25,000 pairs of seismograms that originate from common events, and 25,000 pairs of seismograms that originate from different events. Plotting histograms of the embedding space distances for each pair, as shown in Fig. 7, demonstrates that the distribution for matched-pair distances are considerably lower than the unmatched-pair distances.

We then apply the similarity-based association classifier defined in Eq. (6). The ROC curve for the task has an AUC of 86.8% as shown in Fig. 8. The overall accuracy is 80.0% with a precision and recall of 80.2% and 79.6%, respectively, and our results are nearly identical to the 80% accuracy reported in (McBrearty et al., 2019), extended to much larger network of stations. Performance is also investigated with respect to the distance between recording stations. As noted previously, correlation-based seismogram similarity is known to decay exponentially with an increase in the distance between recording stations. Our path-invariant measure is also negatively affected by increasing this distance, but the effect is much less pronounced, as demonstrated in Table 2.

To further investigate the ability of the embedding space to facilitate event association, Fig. 9, displays 120 seismogram embeddings in 2-dimensions using t-Distributed Stochastic Neighbor Embedding (t-SNE) (Maaten and Hinton, 2008). The figure clearly demonstrates a clustering of embeddings of common events. However, there are obviously other clusters present as well, shown by the dashed lines in the plot. As it turns out, these other clusters can be quite useful, and are explored further in the discussion of the source discrimination task.

The ability of the embedding space to associate regional events across hundreds of stations with 80% accuracy based entirely on waveform similarity is surprising, and begs the question: is the neural network really extracting generalized path-invariant features, or is it merely ‘memorizing’ all the training paths exactly, in a way that appears to support conclusions

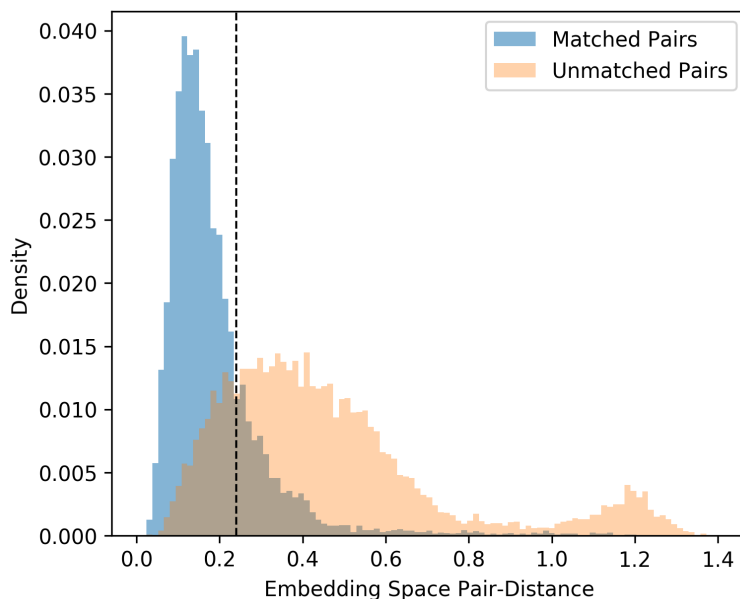


Figure 7: Histograms of matched and unmatched pair distances for the test set. The matched-pair distribution includes embedding space distances for 25,000 pairs of seismograms, where the two embeddings come from the same event. The unmatched-pair distribution includes embedding space distances for 25,000 pairs of seismograms, where the two embeddings come from different events. A cutoff threshold of 0.24 was used to obtain maximum classification accuracy, and is annotated by the dashed line. For this threshold, the area of overlap between the two density plots represents the total classification error, which is  $\sim 20\%$ .

Table 2: Waveform Association Performance vs Inter-station Distance

| Distance (km) | Precision | Recall | Accuracy |
|---------------|-----------|--------|----------|
| 0000-0250 km  | 0.864     | 0.783  | 0.830    |
| 0250-0500 km  | 0.852     | 0.791  | 0.827    |
| 0500-0750 km  | 0.802     | 0.766  | 0.789    |
| 0750-1000 km  | 0.805     | 0.789  | 0.799    |
| 1000-1250 km  | 0.778     | 0.840  | 0.800    |
| 1250-1500 km  | 0.785     | 0.811  | 0.794    |
| 1500-1750 km  | 0.744     | 0.866  | 0.784    |
| 1750-2000 km  | 0.731     | 0.863  | 0.773    |
| 2000-2250 km  | 0.732     | 0.794  | 0.751    |
| 2250-2500 km  | 0.741     | 0.826  | 0.769    |

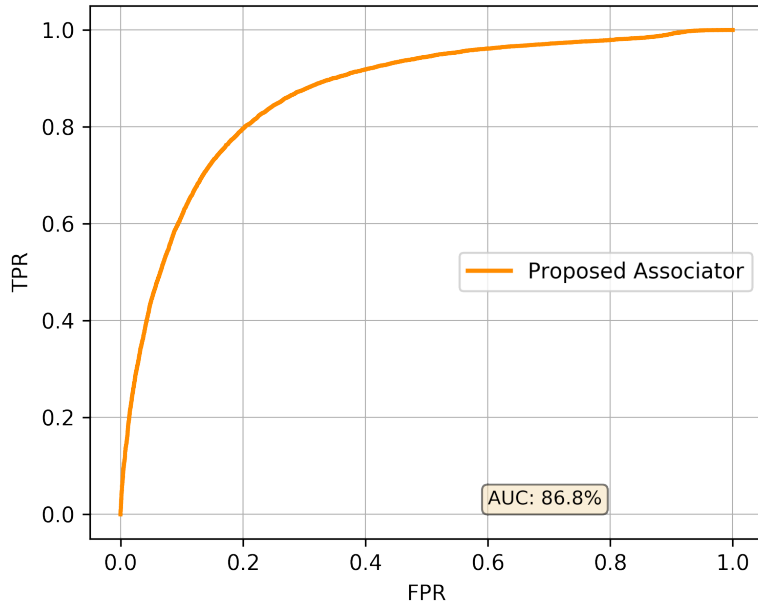


Figure 8: Receiver Operating Characteristic Curve for the Event Association task. The overall area under the curve is 86.8%.

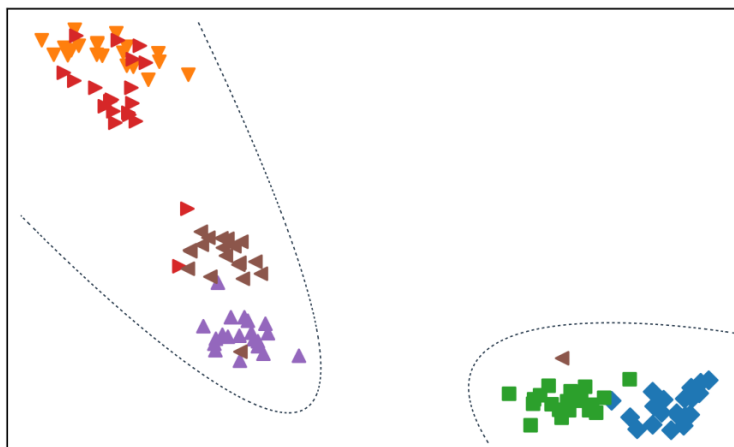


Figure 9: t-SNE Embeddings for Waveform Association. Six unique seismic events were randomly selected from the dataset, along with 20 seismograms for each event, recorded at various stations. These 120 seismograms were then mapped to the 32-dimensional embedding space via the trained neural network. Finally, the 32-dimensional embedding space was visualized here in two dimensions using t-SNE, with each unique event assigned a unique marker. The clustering of same-event embeddings is the result of shared feature commonalities between seismograms of that event. It is interesting to note that there appears to be some aggregate clustering as well, indicated by the dashed lines. This aggregate clustering is the result of feature commonalities shared across seismograms of multiple events. These inter-event commonalities are explored further, in our results for the source discrimination task.



that are unwarranted. To answer this question, we investigate the ability of the embedding space to associate waveforms from novel stations and locations as detailed in Tables 3, 4 and 5. Here, we find that although the performance does drop for such events, the drop is relatively minor. For instance, accuracy only drops from 80% to 79% when considering novel stations, which demonstrates that the neural network has indeed learned to extract features that are invariant to recording location, even novel ones. The accuracy drop is slightly more significant when considering novel event locations, decreasing from 80% to 76% for pairs where at least one event originated near the held-out Rosebud mine. This is understandable, as withholding training events from a certain source location obviously impairs the ability of the neural network to extract features unique to such events at test time.

Table 3: Association Performance for Novel Stations

| <b>Novel STA?</b> | <b>COUNT</b> | <b>ERROR</b> | <b>ACCURACY</b> |
|-------------------|--------------|--------------|-----------------|
| No                | 32221        | 6358         | 0.80            |
| Yes               | 17779        | 3712         | 0.79            |

Table 4: Association Performance for Novel Source Location

| <b>Novel LOC?</b> | <b>COUNT</b> | <b>ERROR</b> | <b>ACCURACY</b> |
|-------------------|--------------|--------------|-----------------|
| No                | 49792        | 10020        | 0.80            |
| Yes               | 208          | 50           | 0.76            |

Table 5: Association Performance for Novel Station and Location

| <b>Novel STA&amp;LOC?</b> | <b>COUNT</b> | <b>ERROR</b> | <b>ACCURACY</b> |
|---------------------------|--------------|--------------|-----------------|
| No                        | 49908        | 10038        | 0.80            |
| Yes                       | 92           | 32           | 0.65            |

## Source Discrimination

To further demonstrate the power of our embedding space, we consider its utility to facilitate template-based source discrimination. The results here are particularly interesting, as the

neural network was not explicitly trained in this task: Although the neural network was exposed to many examples of earthquakes and explosions during training (207,291 and 26,568 respectively), the network had no access to these source labels. However, the network did have access to event labels, and was thus trained to extract features with source-specificity and path-invariance. Unsurprisingly, these source-specific features are well-suited for source discrimination. In Fig. 10, the embedding space is visualized using t-SNE, and labeled by source type, demonstrating a significant separation between the two source classes in the embedding space, with no pre-processing or training.

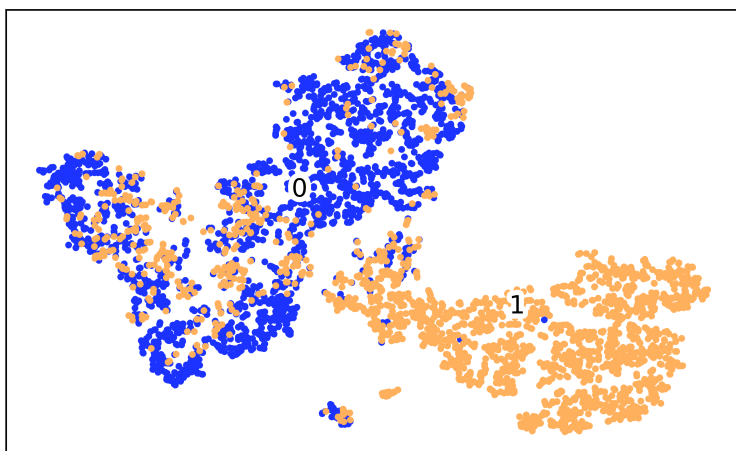


Figure 10: Two-hundred embeddings are shown, visualized in 2D using t-SNE, and labeled according to source function. The light-colored dots represent explosions and the darker dots represent earthquakes; the cluster centroids are annotated by 1 and 0, respectively. The 2D clustering of embeddings demonstrates the inherent association between embeddings with a common source function.

Template-based discrimination performance is demonstrated with three different quantities of randomly-selected exemplar templates: 1, 3 and 10, as shown in Fig. 11. The discriminator achieves a mean AUC of 82.8% for just a single template. This is known as one-shot learning, and enables the creation of a viable classification algorithm with only a single training example. The variance on this AUC is a bit high; however with three templates, this method achieves an AUC of 86.7% with low variance. Choosing the threshold so as to maximize accuracy, the algorithm is then evaluated for accuracy, precision and recall,

which are recorded at 95.8%, 73.4% and 73.6% respectively, which exceeds the performance of the SVM discriminator, but falls just short of the 96.4%, 78.1% and 77.2% performance achieved by a state-of-the-art CNN-based classifier applied to the same dataset, as detailed in Fig. 12. While the CNN technique holds a slight advantage in absolute performance, it must be noted that training the CNN required thousands of labeled explosion waveforms, while the similarity-based method required only a single explosion template. As such, similarity-based source discrimination is only marginally useful against well-studied source types, such as explosions vs earthquakes, where an abundance of extant templates allows the use of traditional machine learning methods. However, similarity-based discrimination holds considerable potential for training future discriminators on more nuanced source functions, especially when training examples are limited and traditional methods are unavailable.

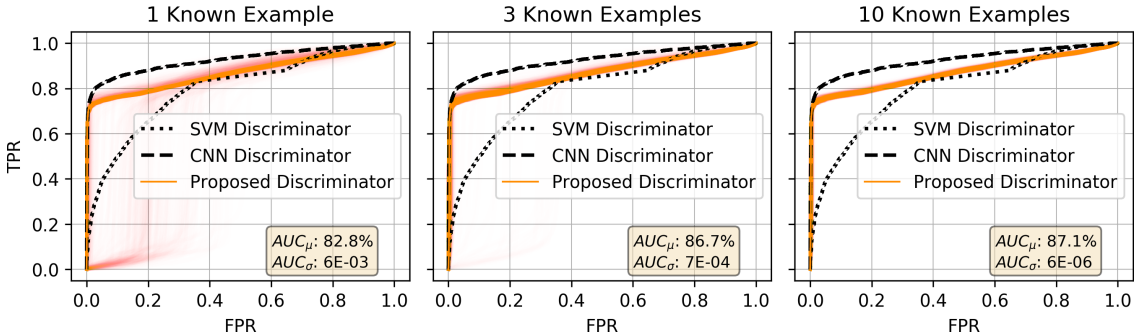


Figure 11: Receiver Operating Characteristic Curves for the Source Discrimination task identifying all explosions. Three plots are shown, demonstrating performance across various numbers of templates (1, 3 and 10). Because the template are chosen randomly, we have performed 1,000 trials for each plot, with the results of each trial plotted as a separate curve. Performance converges nicely for only 3 templates. The dashed and dotted black lines show the performance of two alternative discriminators applied to the same dataset.

## Computation Time

Optimizing the Neural Network during training requires considerable computation time: approximately 30 hours on the aforementioned Nvidia 1080Ti. However the model only needs to be trained once; after training, deployment is quite fast at runtime, requiring only

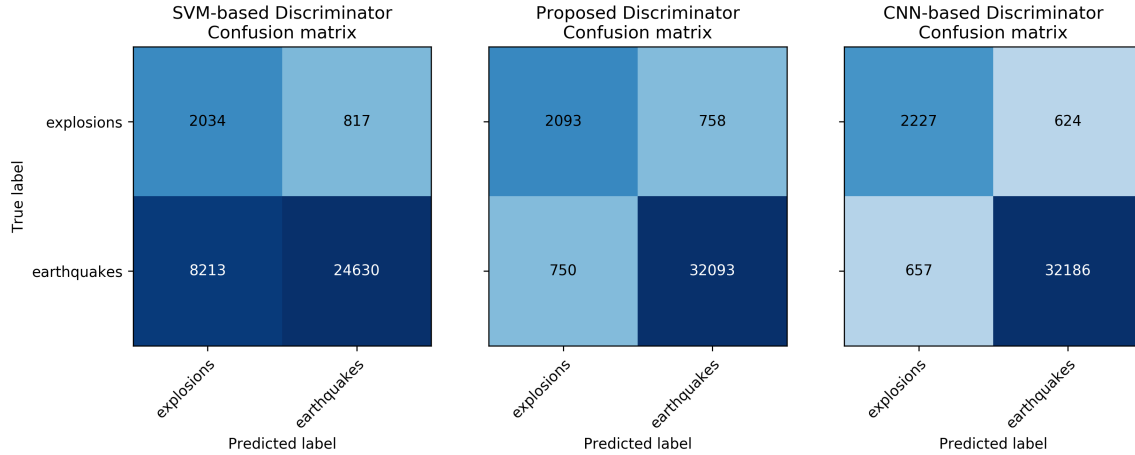


Figure 12: Source Discrimination Confusion Matrix. Three matrices are shown, demonstrating performance of three source discrimination techniques against the test set. Our proposed Similarity-based discriminator utilizes a signal explosion template, whereas the SVM and CNN-based discriminators utilize a large training set with 10,000 labeled earthquakes and 10,000 labeled explosions.

1.8 milliseconds to transform a single 180 second window of 3-channel waveform data onto the embedding space. This represents a four-fold improvement over the 7.6 milliseconds required to take the same waveform and extract the spectrogram features used in traditional source discrimination. Runtimes for the Validation and Test sets are shown in Table 6.

Table 6: Comparison of Runtimes against the Validation and Test Sets

|                                         | <b>Val Set</b><br><b>(22,561 samps)</b> | <b>Test Set</b><br><b>(35,694 samps)</b> | <b>Runtime</b><br><b>per samp</b> |
|-----------------------------------------|-----------------------------------------|------------------------------------------|-----------------------------------|
| Similarity-based NN Embeddings          | 41s                                     | 66s                                      | 1.8ms                             |
| Traditional Spectral Amplitude Features | 171s                                    | 271s                                     | 7.6ms                             |

## CONCLUSION

To date, almost all seismogram similarity measures have been based on the cross-correlation function, constraining them to relatively path-dominant similarity, and limiting their use

to repetitive and geographically localized signals. In this work, we have presented a path-invariant measure for seismogram similarity, based on a deep triplet network architecture. We have demonstrated the effectiveness of this measure for both pairwise event association and template-based source discrimination.

For the event association task, our similarity measure is able to achieve an accuracy of 80%, without any knowledge of recording time or phase type. And while similarity is certainly a weaker evidence for association than a standard moveout curve, it does present a viable complimentary validation tool, which could be used to augment existing methods of event association. In particular, our results show a significant advancement on the work done by McBrearty (McBrearty et al., 2019), both in terms of providing increased generalization and increasing the path distances under consideration. Future work could focus on constructing a framework for a hybrid technique for event association in an operational setting.

The results for the source discrimination task are quite promising. The 95.8% classification accuracy achieved for the explosion vs earthquake task is impressive in its own right. However it is astounding considering that the discrimination is based on a single template waveform. This result is not only useful for the explosion vs earthquake task, but also holds considerable promise for more fine-grained discrimination. For instance, while access to mining explosion templates is extensive, there are other types of anthropogenic events for which we have fewer templates, and it would be interesting to extend these results to such signals. Additionally, future work could also focus on clustering in the embedding space, potentially unveiling new classes of signals.

The findings in this work represent an important step forward in the field of seismogram similarity, demonstrating that such similarity measures do not need to be constrained to the path-dominant correlation-based detectors traditionally implemented.

## Data and Resources

The raw seismograms used in this study were collected as part of Earth Scope’s USArray experiment (Busby et al., 2018), and can be accessed via the Incorporated Research Institutions for Seismology (IRIS) Database using ObsPy (Beyreuther et al., 2010).

Arrival-time catalogs for each station were downloaded through a web query of the International Seismological Centre (ISC) Bulletin for seismic arrivals:

<http://www.isc.ac.uk/iscbulletin/search/arrivals/> (last accessed February 2019).

The Neural Network Architecture was implemented in Keras (Chollet and others, 2015), using the keras-tcn python package written by Philippe Rémy:

<https://github.com/philipperemy/keras-tcn> (last accessed February 2019).

The batch-hard algorithm was implemented in Tensorflow (Abadi et al., 2015), and adapted from the work of Olivier Moindrot, which can be found at:

<https://omoindrot.github.io/triplet-loss> (last accessed February 2019).

## Acknowledgment

The results presented in this paper are solely the opinion of the authors; they do not represent the official position or policy of the United States Government.

## References

- Abadi, M., Agarwal, A., Barham, P., Brevdo, E., Chen, Z., Citro, C., Corrado, G. S., Davis, A., Dean, J., Devin, M., Ghemawat, S., Goodfellow, I., Harp, A., Irving, G., Isard, M., Jia, Y., Jozefowicz, R., Kaiser, L., Kudlur, M., Levenberg, J., Mané, D., Monga, R., Moore, S., Murray, D., Olah, C., Schuster, M., Shlens, J., Steiner, B., Sutskever, I., Talwar, K., Tucker, P., Vanhoucke, V., Vasudevan, V., Viégas, F., Vinyals, O., Warden, P., Wattenberg, M., Wicke, M., Yu, Y., and Zheng, X. (2015). {TensorFlow}: Large-Scale Machine Learning on Heterogeneous Systems.
- Bai, S., Kolter, J. Z., and Koltun, V. (2018). An Empirical Evaluation of Generic Convolutional and Recurrent Networks for Sequence Modeling. *CoRR*, abs/1803.0.
- Beaucé, E., Frank, W. B., and Romanenko, A. (2017). Fast Matched Filter (FMF): An Efficient Seismic Matched-Filter Search for Both CPU and GPU Architectures. *Seismological Research Letters*, 89(1):165–172.

- Belkin, M. and Niyogi, P. (2003). Laplacian Eigenmaps for Dimensionality Reduction and Data Representation. *Neural Computation*, 15(6):1373–1396.
- Bergen, K. J. and Beroza, G. C. (2018a). Detecting earthquakes over a seismic network using single-station similarity measures. *Geophysical Journal International*, 213(3):1984–1998.
- Bergen, K. J. and Beroza, G. C. (2018b). Earthquake Fingerprints: Extracting Waveform Features for Similarity-Based Earthquake Detection. *Pure and Applied Geophysics*.
- Beyreuther, M., Barsch, R., Krischer, L., Megies, T., Behr, Y., and Wassermann, J. (2010). ObsPy: A Python Toolbox for Seismology. *Seismological Research Letters*, 81(3):530–533.
- Bormann, P. and IASPEI (2012). *New Manual of Seismological Observatory Practice (NMSOP-2)*, volume 2 Volumes. GFZ German Research Centre for Geosciences, Potsdam, DE, 2 edition.
- Burges, C. J. C., Platt, J. C., and Jana, S. (2003). Distortion discriminant analysis for audio fingerprinting. *IEEE Transactions on Speech and Audio Processing*, 11(3):165–174.
- Busby, R., Woodward, R., Hafner, K., Vernon, F., and Frassetto, A. (2018). The Design and Implementation of EarthScope’s USArray Transportable Array in the Conterminous United States and Southern Canada. Technical report, Earth Scope.
- C. Pechmann, J. and Kanamori, H. (1982). Waveforms and spectra of preshocks and aftershocks of the 1979 Imperial Valley, California, Earthquake: evidence for fault heterogeneity. *Journal of Geophysical Research*, 871:10579–10598.
- Chen, Y., Garcia, E. K., Gupta, M. R., Rahimi, A., and Cazzanti, L. (2009). Similarity-based Classification: Concepts and Algorithms. *J. Mach. Learn. Res.*, 10:747–776.
- Chollet, F. and others (2015). Keras. [\url{https://keras.io}](https://keras.io).
- Chopra, S., Hadsell, R., and LeCun, Y. (2005). Learning a Similarity Metric Discriminatively, with Application to Face Verification. *Proceedings of the IEEE Computer Society Conference on Computer Vision and Pattern Recognition*, 1:539–546.

- Dickey, J., Borghetti, B., and Junek, W. (2019). Improving Regional and Teleseismic Detection for Single-Trace Waveforms Using a Deep Temporal Convolutional Neural Network Trained with an Array-Beam Catalog. *Sensors*, 19(3).
- Dodge, D. A. and Walter, W. R. (2015). Initial Global Seismic Cross-Correlation Results: Implications for Empirical Signal Detectors. *Bulletin of the Seismological Society of America*, 105(1):240–256.
- Dysart, P. S. and Pulli, J. J. (1987). Spectral study of regional earthquakes and chemical explosions recorded at the NORESS array. Technical report, Center for Seismic Studies.
- Frankel, A. (1982). Precursors to a magnitude 4.8 earthquake in the Virgin Islands: Spatial clustering of small earthquakes, anomalous focal mechanisms, and earthquake doublets. *Bulletin of the Seismological Society of America*, 72(4):1277–1294.
- Giannakis, G. B. and Tsatsanis, M. K. (1990). Signal detection and classification using matched filtering and higher order statistics. *IEEE Transactions on Acoustics, Speech, and Signal Processing*, 38(7):1284–1296.
- Gibbons, S. J. and Ringdal, F. (2006). The detection of low magnitude seismic events using array-based waveform correlation. *Geophysical Journal International*, 165(1):149–166.
- Hadsell, R., Chopra, S., and LeCun, Y. (2006). Dimensionality reduction by learning an invariant mapping. *Proceedings of the IEEE Computer Society Conference on Computer Vision and Pattern Recognition*, 2:1735–1742.
- Harris, D. B. (1991). A waveform correlation method for identifying quarry explosions. *Bulletin of the Seismological Society of America*, 81(6):2395–2418.
- Harris, D. B. (2006). Subspace Detectors: Theory. Technical report, Lawrence Livermore National Laboratory (LLNL), Livermore, CA.
- Hermans, A., Beyer, L., and Leibe, B. (2017). In Defense of the Triplet Loss for Person Re-Identification. *arXiv e-prints*, abs/1703.0.



- Hoffer, E. and Ailon, N. (2015). Deep metric learning using triplet network. *Lecture Notes in Computer Science (including subseries Lecture Notes in Artificial Intelligence and Lecture Notes in Bioinformatics)*, 9370(1271):84–92.
- Hutchings, L. and Wu, F. (1990). Empirical Green’s Functions from small earthquakes: A waveform study of locally recorded aftershocks of the 1971 San Fernando Earthquake. *Journal of Geophysical Research*, 95:1187–1214.
- Israelsson, H. (1990). Correlation of waveforms from closely spaced regional events. *Bulletin of the Seismological Society of America*, 80(6B):2177–2193.
- Jain, P., Kulis, B., Dhillon, I. S., and Grauman, K. (2008). Online metric learning and fast similarity search. *Advances Neural Information Processing Systems*, pages 1–8.
- Jain, P., Kulis, B., V. Davis, J., and S. Dhillon, I. (2009). Metric and Kernel Learning Using a Linear Transformation. *Journal of Machine Learning Research*, 13.
- Jang, D. and Yoo, C. D. (2009). Fingerprint matching based on distance metric learning. In *2009 IEEE International Conference on Acoustics, Speech and Signal Processing*, pages 1529–1532.
- Kanamori, H. and Ishida, M. (1978). The foreshock activity of the 1971 San Fernando earthquake, California. *Bulletin of the Seismological Society of America*, 68(5):1265–1279.
- Koch, G., Zemel, R., and Salakhutdinov, R. (2015). Siamese neural networks for one-shot image recognition. In *ICML Deep Learning Workshop*, volume 2.
- Kong, Q., Trugman, D. T., Ross, Z. E., Bianco, M. J., Gerstoft, P., and Meade, B. J. (2018). Machine Learning in Seismology: Turning Data into Insights. *Seismological Research Letters*, 90(1):3–14.
- Kortström, J., Uski, M., Tiira, T. (2016). Automatic classification of seismic events within a regional seismograph network. *Computers and Geosciences*, 87(1):22-30.
- Kumar, V. B. G., Carneiro, G., and Reid, I. (2016). Learning Local Image Descriptors with Deep Siamese and Triplet Convolutional Networks by Minimizing Global Loss Functions.

- In *IEEE Conference on Computer Vision and Pattern Recognition (CVPR)*, pages 5385–5394.
- Leal-Taixe, L., Canton-Ferrer, C., and Schindler, K. (2016). Learning by Tracking: Siamese CNN for Robust Target Association. *IEEE Computer Society Conference on Computer Vision and Pattern Recognition Workshops*, pages 418–425.
- LeCun, Y., Boser, B., Denker, J. S., Henderson, D., Howard, R. E., Hubbard, W., and Jackel, L. D. (1989). Backpropagation Applied to Handwritten Zip Code Recognition. *Neural Computation*, 1(4):541–551.
- Maaten, L. v. d. and Hinton, G. (2008). Visualizing Data using t-SNE. *Journal of Machine Learning Research*, 9(Nov):2579–2605.
- McBrearty, I. W., Delorey, A. A., and Johnson, P. A. (2019). Pairwise Association of Seismic Arrivals with Convolutional Neural Networks. *Seismological Research Letters*, 90(2).
- Motoya, Y. and Abe, K. (1985). Waveform Similarity among Foreshocks and Aftershocks of the October 18, 1981, Niigata, Hokkaido, Earthquake. In Kisslinger, C. and Rikitake, T., editors, *Practical Approaches to Earthquake Prediction and Warning*, pages 627–636. Springer Netherlands, Dordrecht.
- Nakano, M., Sugiyama, D., Hori, T., Kuwatani, T., and Tsuboi, S. (2019). Discrimination of Seismic Signals from Earthquakes and Tectonic Tremor by Applying a Convolutional Neural Network to Running Spectral Images. *Seismological Research Letters*, 90(2A):530–538.
- Schroff, F., Kalenichenko, D., and Philbin, J. (2015). FaceNet: A Unified Embedding for Face Recognition and Clustering. In *CVPR*.
- Schulte-Theis, H. and Joswig, M. (1993). Master-event correlations of weak local earthquakes by dynamic waveform matching. *Geophysical Journal International*, 113(3):562–574.
- Sidiropoulos, P. (2014). N-sphere chord length distribution. *arXiv preprint*.

- Stauder, W. and Ryall, A. (1967). Spatial distribution and source mechanism of microearthquakes in Central Nevada. *Bulletin of the Seismological Society of America*, 57(6):1317–1345.
- Tibi, R., Young, C., Gonzales, A., Ballard, S., Encarnacao, A. (2017). Rapid and robust cross-correlation-based seismic signal identification using an approximate nearest neighbor method. *Bulletin of the Seismological Society of America*, 107(4):1954-1968.
- Waldhauser, F. and Schaff, D. (2008). Large-scale relocation of two decades of Northern California seismicity using cross-correlation and double-difference methods. *Journal of Geophysical Research: Solid Earth*, 113(B8):0148-0227.
- Wang, J., Song, Y., Leung, T., Rosenberg, C., Wang, J., Philbin, J., Chen, B., and Wu, Y. (2014). Learning Fine-grained Image Similarity with Deep Ranking. *arXiv e-prints*, page arXiv:1404.4661.
- Xing, E. P., Jordan, M. I., Russell, S., Ng, A. Y., Jordan, M. I., and Russell, S. (2002). Distance metric learning with application to clustering with side-information. *Advances in neural information processing systems (NIPS)*, 15(2):505–512.
- Yoon, C. E., O’Reilly, O., Bergen, K. J., and Beroza, G. C. (2015). Earthquake detection through computationally efficient similarity search. *Science advances*, 1(11):e1501057–e1501057.
- Zhang, M. and Wen, L. (2015). An effective method for small event detection: match and locate (MnL). *Geophysical Journal International*, 200(3):1523–1537.

## Mailing Address for Each Author

*Joshua Dickey*

*William Junek*

*Air Force Technical Application Center*

*1020 South Patrick Dr. Bldg 10989*

*Patrick AFB, FL 32925-3516 U.S.A.*

*joshuadickey@gmail.com*

*Brett Borghetti*

*Richard Martin*

*Department of Electrical and Computer Engineering*

*Air Force Institute of Technology*

*2950 Hobson Way*

*Wright-Patterson AFB, OH 45433-7765 U.S.A.*

*brett.borghetti@afit.edu*